Intercalibration of Microwave Radiometer Brightness Temperatures for the Global Precipitation Measurement Mission

Sayak K. Biswas, *Member, IEEE*, Spencer Farrar, *Student Member, IEEE*, Kaushik Gopalan, Andrea Santos-Garcia, *Student Member, IEEE*, W. Linwood Jones, *Life Fellow, IEEE*, and Stephen Bilanow

***Abstract*—A technique for comparing spaceborne microwave radiometer brightness temperatures (Tb) is described in the context of the upcoming National Aeronautics and Space Administration Global Precipitation Measurement (GPM) mission. The GPM mission strategy is to measure precipitation globally with high temporal resolution by using a constellation of satellite radiometers logically united by the GPM core satellite, which will be in a non-sun-synchronous medium inclination orbit. The usefulness of the combined product depends on the consistency of precipitation retrievals from the various microwave radiometers. The Tb calibration requirement to achieve such consistency demands first that Tb's from the individual radiometers be free of instrument and measurement artifacts and, second, that these self-consistent Tb's will be translated to a common standard (GPM core) for the unification of the precipitation retrieval. The intersatellite radiometric calibration technique described herein serves both the purposes by comparing individual radiometer observations to radiative transfer model (RTM) simulations (for "self-consistency" check) and by using a double-difference technique (to establish a linear calibration transfer function from one radiometer to another). This double-difference technique subtracts the RTM-simulated difference from the observed difference between a pair of radiometer Tb's. To establish a linear inter-radiometer calibration transfer function, comparisons at both the cold (ocean) and the warm (land) end of the Tb's are necessary so that, using these two points, slope and offset coefficients are determined. To this end, a simplified calibration transfer technique at the warm end (over the Amazon and Congo rain forest) is introduced. Finally, an error model is described that provides an estimate of the uncertainty of the radiometric bias estimate between comparison radiometer channels.**

Manuscript received January 31, 2012; revised May 18, 2012 and July 15, 2012; accepted July 21, 2012. Date of publication October 25, 2012; date of current version February 21, 2013. This work was supported by a National Aeronautics and Space Administration Headquarters Earth Sciences Division grant for the Precipitation Measurement Mission science team.

S. K. Biswas was with the School of Electrical Engineering and Computer Science, University of Central Florida, Orlando, FL 32816 USA. He is now with the NASA Marshall Space Flight Center, Huntsville, AL 35805 USA (e-mail: sayak.k.biswas@nasa.gov).

S. Farrar, A. Santos-Garcia, and W. L. Jones are with the School of Electrical Engineering and Computer Science, University of Central Florida, Orlando, FL 32816 USA (e-mail: zepplin_32169@yahoo.com; asantosgarcia@gmail.com; ljones5@cfl.rr.com).

K. Gopalan was with the School of Electrical Engineering and Computer Science, University of Central Florida, Orlando, FL 32816 USA, and with the Earth System Science Interdisciplinary Center, University of Maryland, College Park, MD 20740 USA. He is now with the Space Applications Center, Indian Space Research Organization (ISRO), Ahmedabad 380015, India (e-mail: kaubega@gmail.com).

S. Bilanow is with Wyle Information Systems, McLean, VA 22102 USA (e-mail: stephen.bilanow-1@nasa.gov).

Color versions of one or more of the figures in this paper are available online at http://ieeexplore.ieee.org.

Digital Object Identifier 10.1109/TGRS.2012.2217148

***Index Terms*—Global Precipitation Measurement (GPM) Intersatellite Radiometer Calibration Working Group (XCAL), intersatellite radiometric calibration, microwave radiometry.**

I. Introduction

A. Satellite Radiometric Calibration History

THE history of intersatellite radiometric calibration for microwave imagers began with the launch of the first Special Sensor Microwave Imager (SSM/I) on the Defense Meteorological Satellite Program (DMSP) 5D-2 F-8 satellite in June 1987. Prior to this period in the late 1970s through mid-1980s, satellite microwave radiometer imagers developed by the National Aeronautics and Space Administration (NASA) Goddard Space Flight Center were experimental instruments flown on the Nimbus program with no extensive on-orbit radiometric calibration. However, with the launch of the operational SSM/I instruments during the interval of 1987–1997 on DMSP flights F-8 to F-14, the first formal multiyear calibration and validation (Cal/Val) effort was initiated. This work, led by the Space Sciences Division of the Naval Research Laboratory (NRL) in Washington DC, was a postlaunch study to establish the absolute calibration and sensitivity of the instrument and its geolocation accuracy. The results of these first Cal/Val studies were documented in a series of NRL technical reports and journal articles [1]–[4].

An important factor in this intersensor calibration was the fact that the SSM/I instruments were identical in design. This was a tremendous advantage in that the observed radiances (brightness temperatures) for corresponding channels could be directly compared. By making near simultaneous observations of clear-sky (rain-free) ocean scenes over an annual seasonal cycle, this allowed the statistical distributions of brightness temperature to be collected. The analysis of these data permitted the relative radiometric differences (biases) to be determined as a function of the instrument parameters (e.g., temperatures, currents, scan position, etc.). Furthermore, by extending the Cal/Val time series to multiyear, this allowed the time stability of the instrument transfer function and radiometric calibration to be determined. Also, a major radiometric intersatellite calibration activity has been performed by Remote Sensing Systems (RSS) [5] partially under NASA Earth Sciences Division funding. This activity started with SSM/I and continues today, and during this 25-year period, RSS has intersatellite calibrated six SSM/I, two Special

Sensor Microwave Imager/Sounder (SSMIS), WindSat, and Advanced Microwave Scanning Radiometer for the Earth Observing System (AMSR-E) radiometers [6]–[8]. Four important distinctions that set RSS intersatellite calibration activities apart from others are as follows.

1) Intersatellite calibration has been an ongoing process to merge each new radiometer into the existing satellite record. Each generation has been continually updated and improved, and the entire data set has been reprocessed with the current version of calibration.
2) The resulting geophysical retrievals, which are based upon these Tb's, have undergone extensive validation by an international science user community. The excellent consistency found in the intercomparison of the geophysical retrievals between sensors provides a strong argument that the Tb's are also consistent.
3) To achieve radiometric calibration consistency, RSS starts with the original sensor counts rather than brightness temperatures. All on-orbit radiometric calibration adjustments are performed by varying the physical characteristics of the sensor (antenna pattern correction and effective hot load brightness) rather than using *ad hoc* Tb offsets.
4) Finally, since radiometers are very linear instruments, the RSS approach is not dependent upon the scene Tb.

In the mid-1990s, the U.S. federal government decided to merge the military DMSP and the civilian National Oceanic and Atmospheric Administration weather satellite programs. This new program, known as the National Polar-orbiting Operational Environmental Satellite System (NPOESS), was to fly the next generation microwave imager named the Conical Microwave Imager Sounder (CMIS). In support of the CMIS risk reduction activity, the NRL developed the WindSat polarimetric microwave imager [9].

Also, in 1997, as a part of this CMIS risk reduction program, the Central Florida Remote Sensing Laboratory (CFRSL) at the University of Central Florida and the Atmospheric Sciences Department of Texas A&M University collaborated to develop robust intersatellite calibration techniques for the CMIS [10], [11]. The objective of this research was to investigate techniques for cross-calibrating cooperative satellite microwave radiometers and provide consistent brightness temperature calibration. It was recognized that the removal of systematic brightness temperature biases was necessary when producing decadal passive microwave data sets (e.g., SSM/I, SSMIS, AMSR, Tropical Rainfall Measuring Mission (TRMM) Microwave Imager (TMI), and WindSat) for weather and climate research as well as for combining nominally identical sensors such as the multiple copies of CMIS to provide consistent inputs to weather forecast models. Moreover, on-orbit aging of radiometer systems and associated calibration degradation had to be quantified to separate instrumental effects from true changes in environmental parameters. Furthermore, the development of cross-calibration techniques was crucial for extending SSM/I and SSMIS environmental data records using the future NPOESS CMIS. Finally, it was important to extend the previous Cal/Val research performed for SSM/I and the WindSat polarimetric radiometer system to provide the tools necessary for the Cal/Val of CMIS on NPOESS.

B. NASA GPM Mission Intersatellite Calibration Working Group

In March 2007, the Global Precipitation Measurement (GPM) Mission Project Scientist convened a microwave radiometer specialist workshop, which was the formation of the Intersatellite Radiometer Calibration Working Group (a.k.a. XCAL) [12]. The purpose of this *ad hoc* group was to converge on a set of basic approaches to meet the GPM objectives of a single internationally recognized effort to produce an intercalibrated brightness temperature data set. Meeting participants were radio scientists and engineers from federal government and university organizations that were concerned with the on-orbit calibration of microwave radiometers. The organizations endorsed their respective techniques, which were quite different in many respects. After much discussion, it was agreed that this task was quite challenging and that collaboration was advantageous. The following are the five major conclusions from this workshop.

1) The calibration requirements for GPM Level-3 oceanic rainfall retrievals are quite challenging, so it is important that all the constellation radiometers should have a consistent brightness temperature calibration.
2) It is recommended that there be intercomparisons among the various instrument observations as a basis to transform the brightness temperatures to a common virtual calibration standard that is based on a consensus of the available instruments.
3) Furthermore, it is recognized that radiometric calibration, between pairs of satellites, is difficult because there are differences in the channel frequencies and viewing parameters between these instruments. The aim is to develop algorithms that convert one satellite's brightness temperatures to be equivalent to the other or to the virtual instrument representing the consensus calibration (CC).
4) To develop these transforms, the XCAL working group should conduct algorithm intercomparisons using a common data period (July 2005–June 2006) and four sensors to include in the comparison (TMI, WindSat, SSM/I-F13, and SSM/I-F14). Each team should generate transforms that make each of the other three instruments consistent with TMI, and the results should be compared according to agreed-upon metrics.
5) Finally, the XCAL teams should use a common radiative transfer model (RTM) so that the procedures used to generate the transforms can be compared on an unambiguous basis.

Since that initial XCAL meeting five years ago, there has been significant progress, and the procedures have converged to several complementary approaches [13]. This paper describes one of these, namely, the CFRSL XCAL algorithm theoretical basis, and it presents an example of radiometric calibration biases between the TMI and the WindSat polarimetric radiometer.

C. CFRSL XCAL Approach

The CFRSL intersatellite calibration approach is to compare two satellite radiometer observations on a channel

TABLE I
TMI INSTRUMENT PARAMETERS

Center Frequency(GHz)	10.65	19.35	21.3	37.0	85.5
Polarization	V/H	V/H	V	V/H	V/H
Bandwidth(MHz)	100	500	200	2000	3000
Sensitivity(K)	0.63/0.54	0.50/0.47	0.71	0.36/0.31	0.52/0.93
IFOV(km x km)[1]	73x43	35x21	27x21	19x10	8x6
Earth Incidence Angle [1]	53.4°	53.4°	53.4°	53.4°	53.4°

[1]Original specifications [15] adjusted for TRMM mean altitude adjustment from 350 km to 402.5 km in August of 2001.

(frequency/polarization combination) by channel basis utilizing homogeneous Earth scenes that are collocated spatially and temporally. In the simplest sense, if two radiometer channels of identical design were to make an observation over the Earth at the exact same time and space, the difference in their Tb's should reflect the radiometric calibration bias between the satellites. Unfortunately, for radiometers of different design, the situation is more complicated because the scene brightness varies with the observing frequency and viewing geometry (primarily the Earth incidence angle or EIA); therefore, normalization between the sensors is required, before estimating the radiometric bias between the satellites. For the CFRSL method, this normalization utilizes microwave radiative transfer theory to translate the measurement of one or the other to a common basis before comparison.

Thus, the CFRSL intersatellite XCAL procedure involves four steps to find the Tb calibration bias. The first is to calculate the theoretical Tb's for these channels using the RTM with collocated environmental parameters. Next, we take the difference between these theoretical Tb's, which is the expected brightness temperature difference if there were no radiometric calibration biases. The third step is to find the actual difference between the observed Tb's. The final step calculates the double difference of the theoretical Tb difference minus the observed Tb difference, which is the calibration bias between the radiometer channels.

Because the radiometric calibration bias may be a function of observed brightness temperature, a first-order linear correction is implemented that requires that the sensor bias be characterized at both warm and cold scene brightness temperatures. For the cold case, we evaluate sensor biases over homogeneous rain-free global ocean scenes, using the XCAL RTM. For the warm end bias computation, the tropical rainforest, in particular, two densely vegetated regions in Amazon rain forest are chosen [14].

II. DATA SOURCES

A. Satellite Sensor Data

The central goal of this research is to develop an algorithm suitable for GPM intersensor calibration transfer. Also, the calibration algorithm should be able to check the individual consistency of each sensor prior to intersensor comparison. At least two spaceborne sensors are required to apply this algorithm, and to this end, the TMI and the polarimetric radiometer WindSat, on board the Coriolis satellite, are chosen to illustrate the radiometric intercomparison procedure. Since TMI is in a low inclination orbit and WindSat is in a near polar orbit, there are many orbital intersections over a wide range of latitudes to facilitate this intercomparison.

TRMM was launched in November 1997, into a near circular non-sun-synchronous orbit at a 350-km altitude with an inclination of 35°. TMI is a conically scanning total power microwave radiometer, which builds on the heritage of the SSM/I and collects data from an azimuth arc of 130°, resulting in a 759-km swath. This instrument has a total of nine radiometer channels: four dual polarized [vertical (V) and horizontal (H)] measurements at frequencies of 10.65, 19.35, 37, and 85.5 GHz and a single polarization measurement (V-pol) at 21.3 GHz. The instantaneous field of view (IFOV) spatial resolution varies inversely with frequency as given in Table I. The TMI data used herein are the version 7 (v7) of the Level 1B Calibrated Brightness Temperature (Tb) product (i.e., TMI 1B11 v7). The product summary and description for TMI 1B11 could be found in the Goddard Earth Sciences Data and Information Services Center (GES DISC) Web page [16]. The TMI 1B11 has gone through multiple versions/improvements over TRMM's lifetime with the most recent, v7, in 2011. One of the changes from v6 to v7 was the implementation of time-varying solar bias correction [17], [18]. This product can be downloaded using the Mirador Earth Science Data Search Tool [19] developed at the GES DISC.

WindSat is a polarimetric microwave radiometer developed by the NRL Remote Sensing Division and the Naval Center for Space Technology for the U.S. Navy and the NPOESS Integrated Program Office as a risk reduction mission for NPOESS [9]. It was launched on January 6, 2003 on board the United States Air Force Coriolis satellite in an 840-km near circular sun-synchronous polar orbit. WindSat comprises 22 channels operating at five frequencies: 6.8, 10.7, 18.7, 23.8, and 37.0 GHz, of which the 10.7-, 18.7-, and 37.0-GHz channels are fully polarimetric (V/H, $\pm 45°$, and left and right hand circular polarized) with incidence angles ranging from 50° to 55°. WindSat IFOV dimensions (along-track by cross-track) and several instrument parameters are given in Table II. The conically scanning instrument has a forward looking swath of approximately 950 km and an aft looking swath of about 350 km.

Only V- and H-pol measurements from the portion of the WindSat forward swath, which is common among all the frequencies, are used in this study. The WindSat data product used for this research is the WindSat Level 1.1C (L1.1C), which was produced by the Colorado State University. This product was essentially a reformatting of the WindSat sensor data record [20] into the Level 1C brightness temperature product that is designed to be a prototype for GPM.

TABLE II
WINDSAT INSTRUMENT PARAMETERS

Center Frequency(GHz)	6.8	10.7	18.7	23.8	37.0
Polarization	V/H	V/H/±45°/L/R	V/H/±45°/L/R	V/H	V/H/±45°/L/R
Bandwidth(MHz)	125	300	750	500	2000
Sensitivity(K)	0.48	0.37	0.39	0.55	0.45
IFOV(km x km)	60x40	38x25	27x16	20x12	13x8
Earth Incidence Angle	53.5°	49.9°	55.3°	53.0°	53.0°

For our analysis, the raw sensor Tb's are averaged spatially into 1° boxes, which typically have 50–100 samples. For quality control purposes, these boxes are then filtered to remove outliers using the standard deviation of these Tb measurements. Since high standard deviations are indicative of nonhomogeneous environmental conditions, including weather fronts with rain and small island contamination, these boxes are removed when standard deviations exceed 2 K and 3 K for vertical and horizontal polarizations, respectively. For ocean observations, further editing is applied at all frequencies based on the upper limits of brightness temperatures expected from rain-free ocean, and a conservative land mask is also applied to filter out possible Tb contamination from nearby land pixels.

B. Ancillary Data

The modeling of the top of the atmosphere brightness temperatures (Tb) using a microwave RTM is a key procedure in both the cold- and hot-end calibration methods discussed here. For this, we use the NASA XCAL working group's common RTM that requires environmental parameter inputs to simulate Tb's as seen by the spaceborne radiometers. In this paper, we have used two different sets of ancillary data from independent numerical weather prediction (NWP) models and have assessed their impact on the intercalibration results.

The primary data set used here is the National Centers for Environmental Prediction (NCEP) FNL (Final) Operational Global Analyses [21]. This product is from the Global Data Assimilation System (GDAS) that continuously collects observational data from the Global Telecommunications System, and other sources, for many analyses. The FNLs are made using the same model that NCEP uses to create the Global Forecast System. From this point forward, these data will be addressed as GDAS, which is prepared operationally every 6 h on a $1^\circ \times 1^\circ$ latitude/longitude (lat/lon) grid. The grid points are centered at integer values of lat/lon points, including latitude grids at 90° S, 0° and 90° N, resulting in 181×360 grid boxes. The surface environmental parameters are as follows: pressure, sea surface temperature, and 10-m wind speed. The atmosphere environmental parameters are as follows: height profiles of pressure, temperature, specific humidity, and cloud liquid water (CLW). The atmospheric profile data are provided in 26 pressure levels from 1000 to 10 mbar, but for input to our RTM, we only use the first 21 levels between pressures of 1000 and 100 mbar.

For the second environmental input to the RTM, we use the European Centre for Medium-Range Weather Forecasts (ECMWF) Reanalysis Interim (ERA-I) [22], which is the latest ECMWF global atmospheric reanalysis of the period 1979 to present. The data used for this study are available at 1.5° resolution and are interpolated to a standard $1^\circ \times 1^\circ$ grid before being stored in the profile database files. This $1^\circ \times 1^\circ$ grid is composed of 360×180 grid boxes, with the data interpolated to the middle of each grid box. The first grid box is therefore centered at 89.5° S, 0.5° E. There are 29 pressure levels for ERA-I between 1000 and 50 mbar, from which 21 levels are used in our analysis. The time resolution for these ERA-I profile data is the same as that for GDAS, i.e., every 6 h, and the ERA-I environmental parameters are also the same as that for GDAS.

III. RTM

As previously discussed, the CFRSL method for Tb normalization between radiometers of different design utilizes microwave radiative transfer theory to translate the measurement of one or the other to a common basis before comparison. This section describes the NASA Precipitation Measurement Mission science team's Intercalibration Working Group's ocean RTM known as the XCAL RTM.

A. Ocean Surface RTM (Cold End)

The objective of the cold-end calibration is to find the subset of ocean scenes that are homogeneous clear-sky environmental conditions and to use these to establish the relative radiometric calibration bias between two radiometers. When radiometers are of different designs, there may be significant differences in their radiances that are expected and do not necessarily constitute calibration errors. Thus, the use of the RTM allows the expected difference in the scene radiance to be determined.

Unfortunately, the RTM used may not exactly represent the physics of the observation. Also, the RTM input oceanic and atmospheric environmental parameters, derived from numerical weather models, are imperfect estimates of the true values. However, through the use of "double differences" of the theoretical "expected differences" and the "observed differences," these RTM errors will tend to cancel.

The most important characteristic of the RTM is that it accurately captures the dynamic change of the ocean scene radiance due to changes in radiometer frequency, EIA, and polarization as well as changes in environmental parameters. Of the latter, sea surface temperature, wind speed, water vapor, and CLW are the most variable over space and time.

Our assumption is that the radiometer is stable; therefore, the biases should be constants independent of time. To check this, collocations over the one-year seasonal cycle are compared to test this hypothesis. When derived biases are correlated with any of the instrument, orbital or environmental parameters,

then the calibration of the radiometer is considered flawed and must be adjusted to remove the systematic trends before the intersatellite calibration can be performed.

For "clear sky" ocean scenes used in the cold-end calibration, the brightness temperature is dominated by the surface emission. The XCAL RTM uses an ocean surface emissivity module that is based upon specular Fresnel reflection that incorporates an ocean dielectric constant model developed by Meissner and Wentz [23]. This is modified by an additive wind-roughened ocean emissivity model by Elsaesser [24] that uses empirical relationships developed by Wilheit [25], Hollinger [26], and Stogryn [27]. The ocean emissivity model requires sea surface temperature, wind speed, salinity, frequency, polarization, and incidence angle as inputs. It calculates the isotropic ocean surface emissivity and ignores small wind direction effects, which were investigated and found to average to zero globally and have negligible effect on the derived Tb biases. Based upon excellent radiometer wind speed retrievals compared to ocean buoys reported by Wentz [28], there is high confidence in this model to accurately predict ocean emissivity change over wind speed.

B. Atmospheric RTM

Rosenkranz models for water vapor (WV) [29], CLW [30], oxygen (O_2) [31], and nitrogen (N_2) [32] absorption in the atmosphere are used to calculate the atmospheric absorption coefficients. The modules used in the XCAL RTM are available to the public at the XCAL Web site [33]. The largest contribution to the atmospheric absorption in the 18–37-GHz frequency range comes from water vapor. Even though CLW has a significant effect on the Tb simulation for these frequencies, for calibration purposes, the Tb filters used to select boxes usually result in "clear sky" scenes with very low CLW (CLW $<$ 0.1 mm). There is extremely strong O_2 absorption signal near 60 GHz, which does not affect the intercalibration analysis, as our radiometer channels are far removed from that frequency. Thus, WV and CLW are the two atmospheric parameters that significantly affect 10.7–37-GHz frequency emissions. Hence, over the range of frequencies of interest, these two parameters along with Sea Surface Temperature (SST) and wind speed are the four geophysical parameters that significantly impact the RTM-modeled Tb.

The environmental inputs to the RTM are obtained from the ancillary data (GDAS/ERA-I), which provide model outputs at 0000, 0600, 1200, and 1800 Greenwich mean time (GMT) and on a 111-km^2 $(1^\circ \times 1^\circ)$ grid. These data include the atmospheric profiles of various parameters at different pressure levels as well as columnar CLW, sea surface temperature, and ocean wind speed at a 10-m height. The atmosphere is divided into 100 layers of 200-m thickness each; therefore, the atmosphere is modeled up to a height of 20 km, which extends beyond the height of the tropopause [34]. Furthermore, the air in the atmosphere above the tropopause is extremely rarified and does not significantly affect the apparent Tb. Thus, the RTM adequately models the entire extent of the atmospheric contribution to the radiometer Tb. The atmospheric profiles from the ancillary data are interpolated to the heights of the 100 layers in the RTM, using a piecewise linear distribution for temperature and piecewise exponential distributions for pressure and water vapor. The lapse rates of the temperature, pressure, and water vapor have significant differences between the upper and lower layers for some cases. Thus, generating a single fit for the entire vertical profile would have resulted in large resampling errors for these cases. Therefore, piecewise interpolations were used to adequately represent the nonuniform variation of environmental parameters in the different layers.

A uniform distribution is used for CLW, and the heights of the cloud top and bottom are obtained from ocean climatology based on the ENVIMOD model developed by Wisler and Hollinger [35]. It should be noted that the NWP models (GDAS and ERA-I) have cloud layer information, but we have verified that using model-derived cloud boundaries or climatology makes no difference to the mean and standard deviation of the computed Tb's. These environmental parameters are used to calculate the theoretical Tb's for 1° boxes, which are compared to the corresponding means of the Tb observations in each box.

C. Emissivity Model for Tropical Rain Forest (Warm End)

Historically, warm-end radiometric biases have been determined using homogeneous and isotropic land scenes associated with the Amazon tropical rain forest [14]. The near blackbody high emissivity of thick leaf canopy vegetation is almost independent of the measurement polarization, and the observed brightness is very insensitive to the small incidence angle difference among sensors. This enables us to model the surface emissivity as only a function of frequency and use a "double difference" technique to transfer the calibration of one instrument to the other.

The apparent brightness temperature (T_{ap}) at a given frequency measured by a spaceborne microwave radiometer for a given polarization state p can be modeled as

$$T_{ap}^{p} = T_{up} + \tau \times [Surface\ Emission]^{p} \tag{1}$$

where T_{up} is the upwelling brightness temperature of the atmosphere and τ is the atmospheric transmittance (in ratio) for a nonscattering plane parallel atmosphere. These two quantities are easily computed using the atmospheric RTM described in Section III-B of this paper.

On the other hand, the surface emission model depends on the surface type, for example, a specular surface is polarization sensitive while a Lambertian surface is an isotropic scatterer that is completely depolarized. In practice, most of the land surfaces at microwave frequencies are a combination of the aforementioned two types [36]–[38]. To account for the small polarization dependence of satellite-observed Tb's from a tropical rain forest, the surface emissivity is modeled as a linear combination of forest canopy and smooth open water

$$[Surface\ Emission]^{p} = w_{fac} \times Tb_{water}^{p} + (1 - w_{fac}) \times Tb_{surf}. \tag{2}$$

Here, w_{fac} is an estimate of the fractional area of open water present in the observation footprint. It should be noted that,

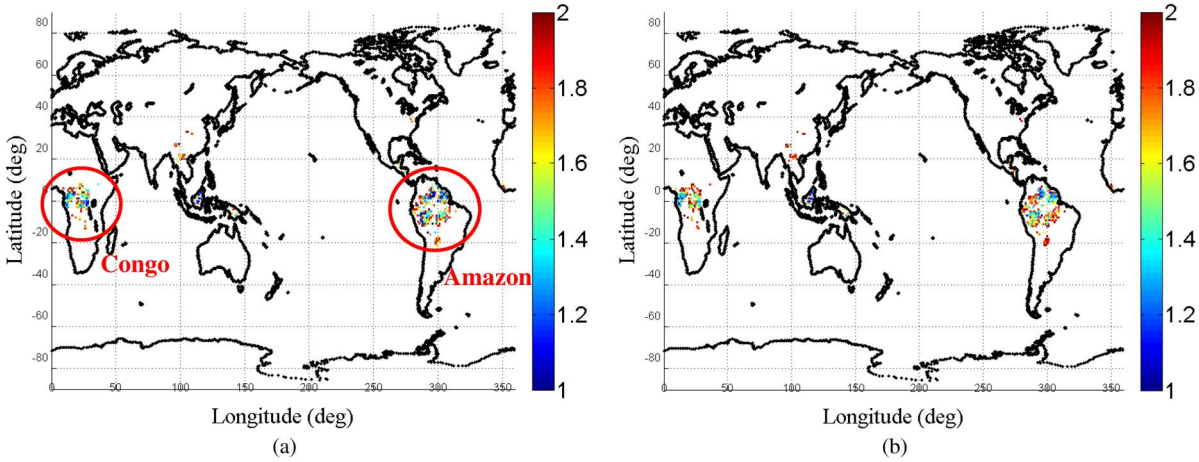

Fig. 1. Global distribution of homogeneous depolarized $1^\circ \times 1^\circ$ lat/lon boxes, with average difference of V- and H-pol Tb's < 2 K, obtained from the observations of (a) TMI and (b) WindSat. The color bar represents the extent of depolarization in terms of 10.7-GHz V-pol minus H-pol Tb difference.

for calibration purpose, we are looking at a nearly unpolarized scene with the difference in the V-pol (T_v) and the H-pol (T_h) Tb being less than 2 K. Our model treats this small polarization sensitivity of the scene to be the result of open water in the sensor footprints. Therefore, w_{fac} is derived from the normalized difference between the observed V- and H-pol Tb's and the land surface temperature (T^{ph}_{surf}) value from GDAS. Thus

$$w_{fac} = (T_v - T_h)/T^{ph}_{surf}. \tag{3}$$

In (2), Tb^p_{water} is the specular brightness temperature from fresh water at zero wind speed for a given polarization. It is computed using the emissivity model [23], [39] assuming the water physical temperature to be equal to T^{ph}_{surf}. The quantity Tb_{surf} in (2) is the emission of the dense forest canopy. According to Karbou and Prigent [36], for any surface type, the specular assumption is valid for conical scanners with an incidence angle close to 53° (which is the case for WindSat and TMI). Thus, we model the Tb_{surf} as

$$Tb_{surf} = e_{surf} \times T^{ph}_{surf} + (1 - e_{surf}) \times T_{dn} \tag{4}$$

where e_{surf} is the unpolarized emissivity of a weakly scattering canopy over soil where e_{surf} is completely depolarized and has no incidence angle dependence. The downwelling atmospheric emission, T_{dn}, is computed using GDAS/ERA-I profiles. Equations (1)–(4) complete the forward model to compute the top of the atmosphere Tb at a given frequency and polarization. In these equations, the only unknown quantity is e_{surf}, which is supplied as *a priori* information.

The TMI and WindSat data described in Section II-A of this paper are used for the empirical derivation of e_{surf}. Both instruments are collocated globally, in $1^\circ \times 1^\circ$ lat/lon boxes and within a ±60-min time window. The XCAL radiometer observation data set spans the time period from July 2005 to June 2006. To select depolarized regions, a brightness temperature filter is applied, which selects Tb boxes with 0 K $\leq T_v - T_h \leq$ 2 K and $w_{fac} \leq 0.01$. The $1^\circ \times 1^\circ$ boxes are filtered based on homogeneity by checking the standard deviation (std) among all the measured pixel Tb's within that box. Only the boxes where the V-pol Tb std $\leq$ 2 K and H-pol Tb std $\leq$ 3 K are kept for the estimation of e_{surf}.

The global maps for these depolarized boxes are plotted in Fig. 1. Panel (a) shows the filtered boxes obtained from TMI data, and panel (b) shows the same for WindSat. The color bar represents the extent of depolarization in terms of 10.7-GHz Tb difference $(T_v - T_h)$ in kelvin. It should be noted that our filters effectively output land regions with thick vegetation, for example: the Amazon Basin; Congo Basin of equatorial Africa; and East Indies, from Sumatra to New Guinea. Three special regions are chosen for emissivity retrieval—Amazon-1 ($5^\circ - 10^\circ$ S and $65^\circ - 74^\circ$ W) and Amazon-2 ($1^\circ - 4^\circ$ N and $53^\circ - 59^\circ$ W) described in [14] and a region in Congo within $1^\circ - 3^\circ$ N and $15^\circ - 17^\circ$ E.

The unpolarized emissivity (e_{surf}) is then derived for each channel of WindSat and TMI separately by inverting the forward model described in (1)–(4). In Fig. 2, the retrieved emissivity is plotted separately for V-pol [panel (a)] and H-pol [panel (b)] channels. Three regions are separated by colors: Amazon 1 (red), Amazon 2 (blue), and Congo (green). It should be noted that the 85-GHz channel of TMI has the largest uncertainty associated with the retrieved emissivity. This is due the fact that the RTM has several limitations at those high frequencies including the lack of atmospheric scattering from water and ice clouds. In general, Fig. 2 demonstrates the polarization independence of our retrieved emissivity. Also, the small incidence angle difference between WindSat and TMI channels is not causing any statistically significant error in emissivity values. Hence, it is possible to model this emissivity as only a function of frequency. All the retrievals are combined for Amazon regions and Congo, and a best fit polynomial expression for the emissivity is obtained and is shown in Fig. 3. The red stars are retrievals from TMI, and blue boxes are from WindSat. It should be noted that, in Fig. 3, for any dual polarized channel, there are six closely placed retrieval points—which are retrieved emissivities for V-pol and H-pol in Amazon regions 1 and 2 and Congo (a total of six). The black line is the best fit polynomial given by

$$e_{surf} = p1 \times (log_e(f))^2 + p2 \times log_e(f) + p3 \tag{5}$$

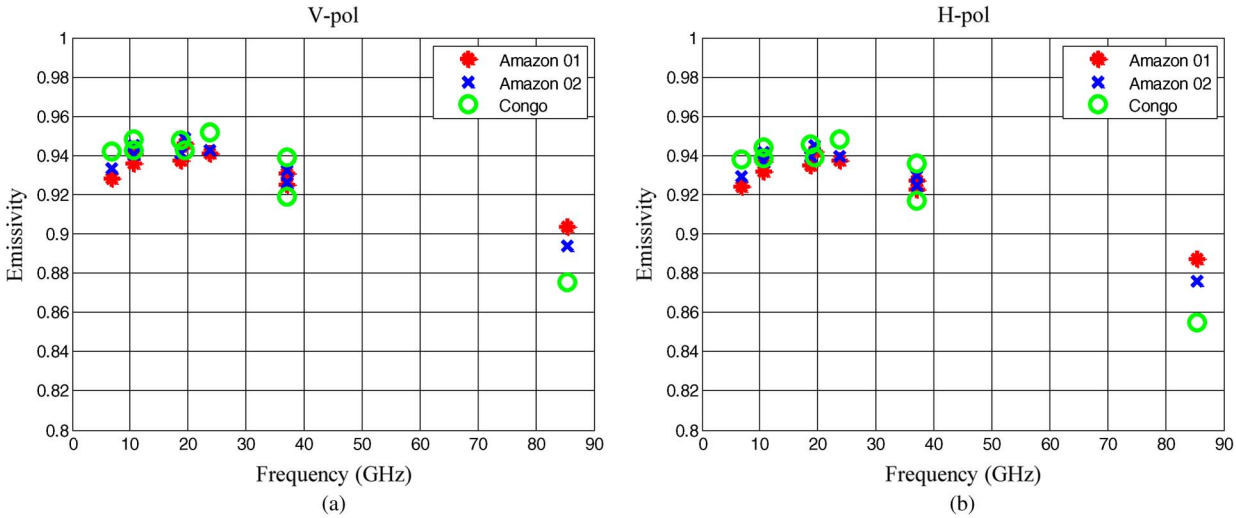

Fig. 2. Retrieved unpolarized emissivity (e_{surf}) of a weakly scattering canopy over soil derived from both TMI and WindSat using observed (a) V-pol Tb's and (b) H-pol Tb's. The mean emissivity is plotted separated by three regions: (Red) Amazon-1, (blue) Amazon-2, and (green) Congo.

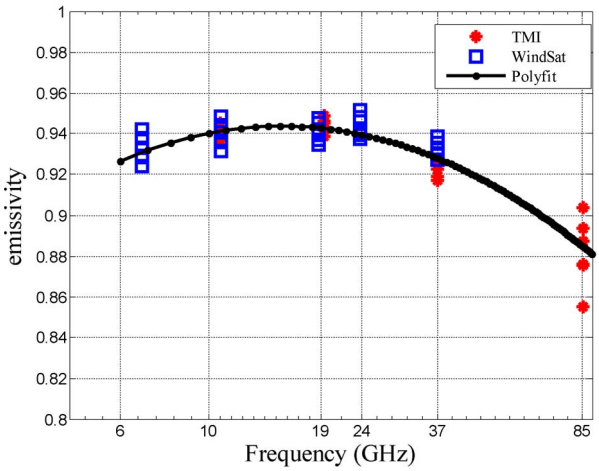

Fig. 3. Derived emissivity (e_{surf}) of weakly scattering canopy over soil as a function of frequency of observation, combining all channels of (red) TMI and (blue) WindSat. The frequency axis is plotted in logarithmic scale. (Black) Second-order fit against the frequency (in gigahertz) in natural logarithm domain is used to represent the frequency dependence of this unpolarized emissivity.

TABLE III
AMAZON EMISSIVITY COEFFICIENTS [SEE (5)]

p1	p2	p3
-0.019854	0.10800	0.79689

where f is the frequency in gigahertz. The values for p1, p2, and p3 are given in Table III.

The sole purpose of (5) is to capture the frequency dependence of the unpolarized emissivity. In our technique, we treat the Amazon as a transfer standard and NOT an absolute calibration standard. First-order error in absolute calibration will cancel out by the use of double-difference technique (described in Section IV). Hence, this method is used as a calibration transfer for obtaining relative bias between two satellite instruments. The fact that the retrieved emissivity (in Fig. 3) increases up to 10 GHz and then starts decreasing monotonically is physically realistic. For example, Isaacs *et al.* [40] developed a model for the emissivity of a heavily vegetated scene based on radiative transfer through a continuous random media. They determined that, for optically thick (i.e., water laden) vegetation, the emissivity increased with frequency up to 10 GHz and then monotonically decreased with frequency thereafter. This behavior results because, once the optical depth of the canopy becomes large enough to obscure emission from the surface (which occurs near 10 GHz for a thick canopy), any further increase in frequency tends to increase the scattering by the canopy, which will lower the effective emissivity of the surface plus canopy. Above 10 GHz, the emissivity modeled by Isaacs *et al.* [40] was also unpolarized and had little angular dependence. A more recent model for the emissivity of a leafy deciduous forest also showed saturation effects at 10 GHz for high biomass content [41]. This phenomenon is also addressed in [14].

IV. ALGORITHM

A. Sensor Self-Consistency Check

Radiometers included in GPM constellation are "pre-screened" for calibration irregularities. Our method involves collocating 1° brightness temperature grids (see Section II-A of this paper) with ancillary data. The $1^\circ \times 1^\circ$ Tb grids are generated per orbit basis for each sensor, for each radiometer channel. The average time of all the observations falling in a 1° box is assigned as the observation time of that box. There are four environmental parameter files per day, generated at 00, 06, 12, and 18 h GMT. A file with time within ±3 h of the box observation time is chosen for collocation.

Let us consider that the average Tb for a particular channel, observed by a sensor in a 1° box, is Tb_{obs}. Depending on whether it is a cold- or warm-end comparison, an appropriate RTM is run (see Section III) using the collocated environmental parameters and given sensor parameters (frequency, incidence angle, and polarization). If the RTM output Tb is

represented by Tb_{rtm}, then the single-difference bias (B_{SD}) is computed as

$$B_{SD} = Tb_{obs} - Tb_{rtm}. \quad (6)$$

Ideally, for all the radiometer sensors in the GPM constellation, we expect the B_{SD} statistic to be normally distributed with zero mean. However, since the RTM input parameters are only an estimation of the true geophysical scene under observation and since the RTM (physics and absorption coefficients) is not perfect, absolute biases may be present in the simulated brightness temperatures. Therefore, a nonzero mean of B_{SD} in (6) does not necessarily point to an absolute calibration error.

Even though the mean of B_{SD} does not help us in estimating absolute calibration errors, it can be further analyzed to determine if the sensor is consistent with itself. For example, the B_{SD} is checked for possible correlation with several instrument and flight parameters: scan position, solar heating (sun beta angle), orbit phase, distance from landmass, ascending/descending node time (for sun-synchronous satellites), etc. If a significant correlation is found, a correction is introduced before accepting the instrument for intercalibration.

We have successfully demonstrated this technique for TMI solar bias correction in [17] and [18]. Also, a two-point calibration technique using B_{SD}'s, to correct for beam spoiling of the spaceborne radiometers, is described by McKague *et al.* [42]. Using a combination of vicarious cold [43] and warm [14] calibration techniques applied on WindSat data, they demonstrated that the brightness temperature can be corrected for attitude offsets as well as beam spoiling due to interference from onboard sources (cold sky reflector and hot load) near the radiometer edge of scan. The magnitude of the roll and pitch offset of the instrument as well as the beam fractions and effective radiating temperatures of the onboard obstructions were also estimated.

B. Intersensor Calibration

To perform the second GPM calibration goal of intersatellite calibration transfer, B_{SD}'s from a pair of satellites are compared. The bias for an arbitrary sensor-A with respect to another sensor-B is given by the double difference of individual B_{SD}'s

$$\begin{aligned} B_{DD}(AB) &= B_{SD}(A) - B_{SD}(B) \\ &= (Tb_{obs} - Tb_{rtm})_A - (Tb_{obs} - Tb_{rtm})_B. \end{aligned} \quad (7)$$

The terms in (7) can be rearranged to represent the bias of sensor-A with respect to sensor-B as a single-difference term

$$B_{DD}(AB) = (Tb_{obs})_A - (Tb_{pred})_{AB} \quad (8)$$

where $(Tb_{pred})_{AB}$ is the predicted Tb of sensor-A based on the observation made by sensor-B and is given by

$$(Tb_{pred})_{AB} = (Tb_{obs})_B + (Tb_{rtm})_A - (Tb_{rtm})_B. \quad (9)$$

The second term in the right-hand side of (9) is a difference in the RTM Tb's of sensors A and B. This difference essentially cancels out any absolute bias that may exist in the RTM and provides us with an estimate of the theoretical difference between the observed Tb's due to difference in sensor parameters (e.g., frequency and incidence angle) only.

It should be noted that the double difference only cancels first-order RTM biases which are linear with relevant parameters. The second-order errors will still show up in the double difference. This will be particularly important around the 23-GHz water vapor absorption line and at higher frequencies where water vapor continuum absorption becomes significant for scenes with appreciable total precipitable water. This second-order effect is minimized by the choice of "clear" ocean scenes with negligible total precipitable water.

Adding the theoretical difference to the sensor-B-observed brightness temperature $(Tb_{obs})_B$ produces a theoretical prediction of sensor-A Tb. Furthermore, if sensor-B is known to be well calibrated and demonstrated to be self-consistent, then a more robust method is to use $B_{DD}(AB)$ (instead of $B_{SD}(A)$) for checking sensor-A self-consistency.

In the GPM scenario, all constellation radiometers will be cross-calibrated against the GPM Microwave Imager (GMI), and GMI will serve as a calibration standard. The B_{DD} between GMI and any other constellation radiometer, computed for "cold" (ocean) Tb's and "warm" (rain forest) Tb's, will provide a linear transfer function between the two. This technique will be used to transfer the calibration of GMI (or the "consensus standard") to any constellation member.

V. Results

Because of the non-sun-synchronous orbit of TRMM, the TMI instrument is chosen as a "proxy" for GMI in the current cross-calibration algorithm development effort of the XCAL group [13]. However, recent TMI intercomparisons with WindSat and SSM/I F-13 and F-14 by Gopalan *et al.* [17] have uncovered a time-varying radiometric bias in TMI. Even though our empirical correction [18] in the v7 of the TMI 1B11 Tb product [16] effectively corrects the bias, this finding reduced the confidence in selecting the TMI instrument as the XCAL calibration standard.

After considerable deliberation by the XCAL group, it was agreed that, if the calibration of each instrument in the GPM constellation is independent, then an appropriately weighted average would result in a better calibration rather than selecting any single radiometer as the standard. As a result, a linear combination of TMI and WindSat was adopted as the "CC" as described by Wilheit *et al.* [13]. This involved the combination of radiometric bias estimates by independent techniques contributed by XCAL working group members. Since the CFRSL approach is one of these techniques, it is necessary that we provide an uncertainty estimate in our radiometric biases to establish an objective weighting for the consensus.

A major contributor to this uncertainty estimate involves the assumption that the double-difference technique effectively removes the influence of the RTM on the estimated biases. The XCAL RTM is believed to be state of the art for the physics associated with ocean surface emissivity and a nonscattering atmospheric transmission/emission for the microwave window

TABLE IV
TMI SINGLE DIFFERENCES (COLD END)

	Mean(K)				Std(K)			
	10 V/H	**19 V/H**	**22V**	**37V/H**	**10 V/H**	**19 V/H**	**22V**	**37V/H**
GDAS	0.31/-1.24	1.12/0.60	-0.04	-1.80/0.39	0.63/0.90	1.28/2.29	2.01	1.54/2.89
ERA-I	0.31/-1.12	1.61/1.67	1.11	-2.30/-0.22	0.73/2.03	1.32/3.10	1.93	1.60/3.81
Difference	0.00/-0.12	-0.49/-1.07	-1.15	0.50/0.61				

TABLE V
WINDSAT SINGLE DIFFERENCES (COLD END)

	Mean(K)				Std(K)			
	10 V/H	**19 V/H**	**22V**	**37V/H**	**10 V/H**	**19 V/H**	**22V**	**37V/H**
GDAS	0.05/0.38	1.68/3.44	1.73	1.43/2.90	0.61/0.87	1.15/2.17	1.98	1.54/2.91
ERA-I	0.08/0.50	1.98/4.27	2.73	0.93/2.28	0.77/1.97	1.15/3.02	1.92	1.59/3.80
Difference	-0.03/-0.12	-0.30/-0.84	-1.00	0.50/0.61				

channels ($<$ 100 GHz). However, it is recognized that the use of numerical weather models to provide the environmental parameters to drive the RTM is not perfect.

To establish the sensitivity of our method to these environmental parameters, we have used two different ancillary NWP model data sets, viz., GDAS and ERA-I (see Section II-B for details). This analysis is performed only over ocean. The mean and standard deviation of single-difference biases (B_{SD}) are obtained after applying a Gaussian fit to the raw bias histograms and filtering the outliers. These results are tabulated in Table IV for TMI. The mean bias values fall within a range of 4.97 K (between -2.30 K to $+1.67$ K) for all the channel errors combined, and the std's represent how well the RTM Tb's match the observations. In general, it is evident that the V-pol std's for TMI B_{SD} are smaller in magnitude than those for H-pol. This does not necessarily mean that the RTM agrees best with the V-pol observations because it is possible that the V-channel's smaller dynamic range reduces the std's. Another notable observation is the difference between GDAS and ERA-I std values. Except for the 22-GHz V-pol channel, GDAS std's are generally smaller compared to that of ERA-I.

The same parameters are tabulated for WindSat channels in Table V. Here, the dynamic range of total bias variation across all the channels of WindSat is 4.22 K with the minimum at 10-GHz V-pol using GDAS profiles and the maximum at 19-GHz H-pol using ERA-I profiles. The std's behave in a similar way as that of TMI, reinforcing the fact that GDAS profiles fit the observations better than the ERA-I ones. As mentioned earlier B_{SD}'s might have absolute calibration offsets due to the limitations of RTM and ancillary input parameters; thus, we explore further the effect of input profiles in the "double difference" (B_{DD}).

Table VI shows the B_{DD} biases of TMI with respect to WindSat along with the mean "cold" Tb of TMI at which they were observed. For the GDAS input, the biases vary between -3.23 K (37-GHz V-pol) and $+0.26$ K (10-GHz V-pol), and the variation is approximately the same for ERA-I. One encouraging result is that the BDD is insensitive to changing ancillary inputs to the RTM. Also, the std's are reduced by more than 50% by most of the channels. Note that, even

TABLE VI
TMI–WINDSAT DOUBLE DIFFERENCES (COLD END)

	Mean[K] /Std [K] (GDAS)	**Mean[K] /Std [K] (ERA-I)**	**@Tb[K]**
10V	0.26/0.30	0.23/0.32	170
10H	-1.62/0.38	-1.62/0.38	88
19V	-0.56/0.58	-0.37/0.62	199
19H	-2.84/0.82	-2.60/0.83	132
22V	-1.77/0.66	-1.62/0.66	219
37V	-3.23/0.58	-3.23/0.58	214
37H	-2.51/0.91	-2.51/0.91	152

though the B_{SD} std's are larger in ERA-I than in GDAS, the corresponding B_{DD} std's are almost exactly the same. This means that the larger fitting errors in B_{SD} using ERA-I between TMI and WindSat are correlated and cancel out in the B_{DD} technique. This demonstrates the robustness of the double-difference algorithm.

To arrive at a single uncertainty estimate in our cold-end bias (by channel), we group the bias values by month, ascending/descending phase of the orbit, and for two different sets of input environmental parameters (GDAS and ERA-I). In this way, 24 monthly averaged independent estimates of the bias are obtained for each set of environmental input. As an example, TMI 10- and 19-GHz biases for both V-pol and H-pol separated by each month between July 2005 and June 2006 are plotted in Fig. 4. The red (ERA-I) and blue (GDAS) colors separate the ancillary data set used to obtain the biases. The ascending and descending bias estimates are combined to a single mean bias for each month and for each set of environmental input. At 10 GHz [see Fig. 4(a)], the bias looks very stable from month to month for both the polarizations. However, at 19 GHz (a frequency close to the WV resonance line near 22 GHz), the bias estimates seem to deviate more from month to month and also within a month among GDAS and ERA-I inputs. The WV uncertainties in the ancillary data and the RTM's sensitivity to it near 22 GHz are two major reasons for such a fluctuation in bias estimates. To estimate uncertainties, we compute the standard deviation among the 24 means for GDAS and ERA-I

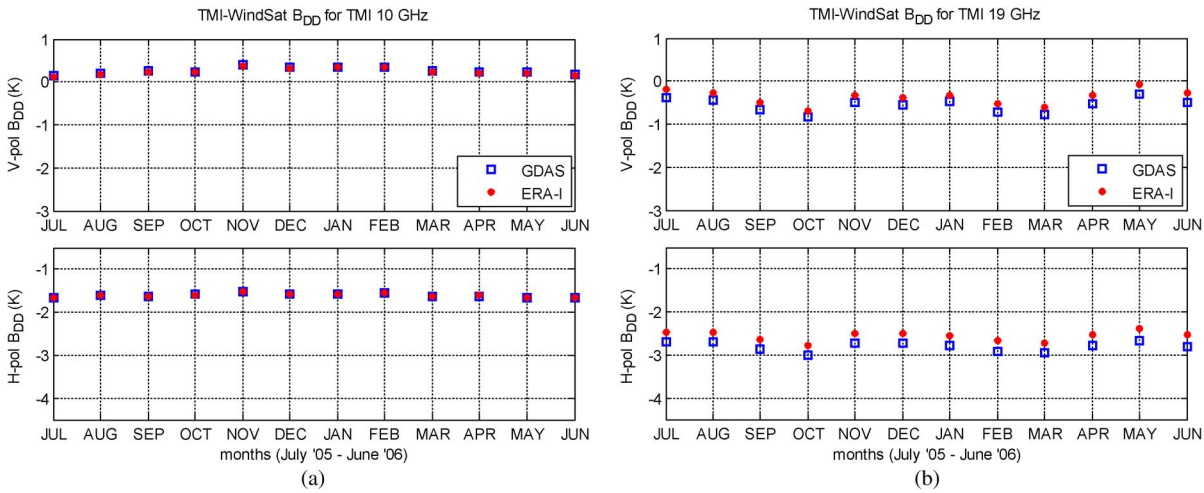

Fig. 4. Monthly average TMI–WindSat double-difference bias time series at cold end between July 2005 and June 2006 for (a) 10-GHz and (b) 19-GHz TMI channels. The biases are computed separately using (blue) GDAS and (red) ERA-I environmental parameter inputs to the XCAL RTM. (a) 10-GHz biases using (blue) GDAS and (red) ERA-I. (b) 19-GHz biases using (blue) GDAS and (red) ERA-I.

TABLE VII
TMI–WINDSAT MONTHLY B_{DD} STANDARD DEVIATIONS (COLD END)

	10 V/H	19 V/H	22 V	37 V/H
GDAS	0.084/0.095	0.167/0.281	0.135	0.148/0.159
ERA-I	0.088/0.097	0.184/0.286	0.139	0.148/0.158

TABLE VIII
COLD END B_{DD} BIAS UNCERTAINTIES (95% CONFIDENCE INTERVAL)

	10 V/H	19 V/H	22 V	37 V/H
ΔB_{DD}	±0.12/±0.14	±0.25/±0.40	±0.19	±0.21/±0.22

TABLE IX
TMI–WINDSAT DOUBLE DIFFERENCES (WARM END)

	Mean[K]/Std [K]	@Tb[K]
10V	-1.06/0.72	282
10H	-0.89/0.67	280
19V	-0.77/0.76	285
19H	-1.08/0.76	284
22V	-3.00/0.61	284
37V	-3.31/0.64	281
37H	-3.00/0.64	281

inputs separately. The std values are tabulated in Table VII, and the value for 19 GHz is found to be the worst case among all four frequencies.

Finally, to estimate the uncertainties in each channel bias, we treat the biases computed using GDAS and ERA-I as two independent estimates. Therefore, the standard deviations are combined as

$$\sigma_{tot} = \left(1/\sigma^2_{GDAS} + 1/\sigma^2_{ERA-I}\right)^{-\frac{1}{2}} \tag{10}$$

where σ_{tot} is the total standard deviation combining estimates from GDAS (with std σ_{GDAS}) and ERA-I (with std σ_{ERA-I}). The 95% confidence intervals of our bias estimations (equivalent to two std) are given in Table VIII. The lowest and the largest uncertainties are at 10 and 19 GHz, respectively.

The warm-end (Amazon and Congo) targets are not as spatially uniform as the cold end, and they have a strong diurnal Tb signature. Collocation boxes with nonhomogeneous Tb scene are detected based on the standard deviation of the observed Tb values within the box and removed from the data set before computing bias. This method significantly reduces the number of 1° boxes available to estimate biases. Also, to minimize the effect of the diurnal Tb signature, we restrict the collocation times to ±1 h and apply an adjustment to the TMI Tb's to compensate for local time differences compared with the constant time of day observations of WindSat. This also results in a reduced number of boxes available for statistical analysis. Therefore, compared to the ocean bias determination, the uncertainties associated with land are considerably larger; nevertheless, the ability to produce an uncertainty estimate makes the hot-end bias results statistically significant.

The warm-end double-difference bias values are reported in Table IX along with the associated observed TMI brightness temperatures. These biases are computed using GDAS environmental input parameters. As expected there is not much variation of the average warm-end temperature across the channels compared to the TMI Tb's reported in Table VI, because of the depolarized nature of the chosen target (Amazon rain forest). The computed biases between TMI and WindSat vary between −3.31 K at 281 K (37-GHz V-pol) and −0.77 K at 285 K (19-GHz V-pol).

To compute the uncertainties in the warm-end bias estimates, a method similar to the cold end is followed. Fig. 5 compares the monthly average bias time series between the cold and the warm end for 10- and 19-GHz channels. For both V- and H-pol channels at 10 GHz [see Fig. 5(a)], the warm-end bias shows a greater month-to-month variation compared to the bias at the cold end. For the 19-GHz V-pol channel [see Fig. 5(b)], the magnitude and shape of the monthly variation are more or less equal, whereas for the corresponding H-pol channel, the warm-end results are more varying than the cold-end ones. One interesting observation is that the shape of the month-to-month

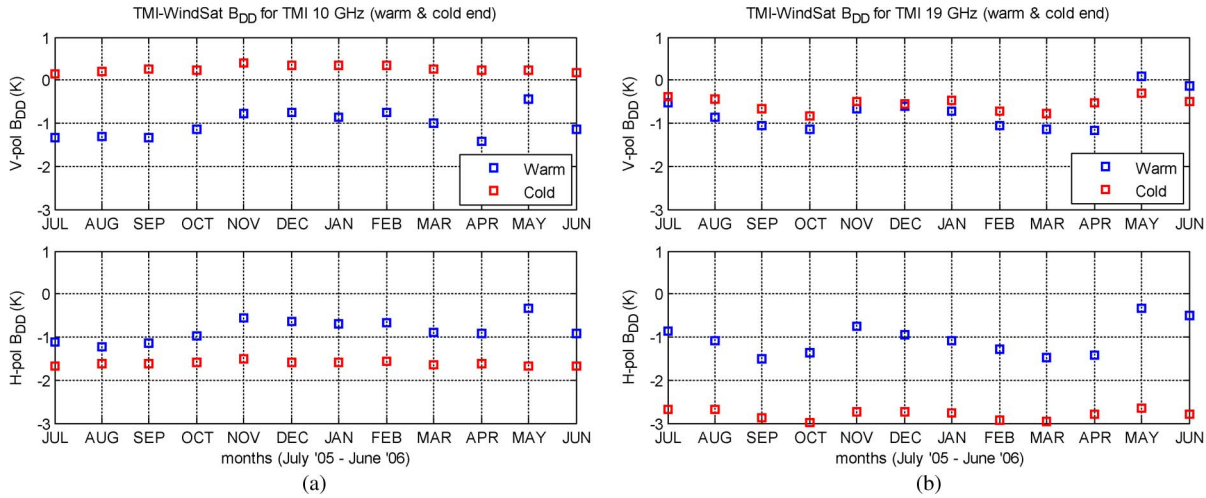

Fig. 5. Monthly average TMI–WindSat double-difference bias time series for warm- and cold-end comparisons between July 2005 and June 2006 for (a) 10-GHz and (b) 19-GHz TMI channels. The (blue) warm-end and (red) cold-end biases are separated using colors. GDAS environmental parameters are used as input to the XCAL RTM for both cases. (a) 10-GHz biases at warm and cold ends. (b) 19-GHz biases at warm and cold ends.

TABLE X
TMI–WINDSAT MONTHLY B_{DD} STANDARD DEVIATIONS (WARM END)

10 V/H	19 V/H	22 V	37 V/H
0.309/0.269	0.409/0.386	0.237	0.282/0.305

TABLE XI
WARM END B_{DD} BIAS UNCERTAINTIES (95% CONFIDENCE INTERVAL)

	10 V/H	19 V/H	22 V	37 V/H
ΔB_{DD}	$\pm$0.62/$\pm$0.54	$\pm$0.82/$\pm$0.77	$\pm$0.47	$\pm$0.56/$\pm$0.61

B_{DD} variations is highly correlated between both warm- and cold-end cases even though the peak-to-peak variation is more at the warm end. The standard deviations for these 12 monthly means are tabulated in Table X. Similar to the cold-end case in Table VII, the 19-GHz frequency is found to have the worst std error. The 95% confidence intervals of our warm-end bias estimations are given in Table XI.

VI. CONCLUSION

A technique for comparing spaceborne microwave radiometer brightness temperature calibrations is described in the context of the upcoming GPM mission. The GPM algorithm requires Tb biases to be computed at both "cold" and "warm" ends of the observed Tb dynamic range. To this end, two microwave RTMs, over ocean (cold) and the Amazon and Congo rain forest (warm), are presented. Single (B_{SD}) and double (B_{DD}) difference techniques for bias estimation are described, and example results are provided using TMI and WindSat radiometers with two sets of ancillary NWP model environmental parameter inputs (GDAS/ERA-I). The robustness of B_{DD} over B_{SD} is shown in the final results. The comparison between GDAS and ERA-I revealed that the technique is not sensitive to the use of a different set of ancillary data. Also, warm-end B_{DD} biases for TMI with respect to WindSat are presented, and finally, an error estimation is also presented for both the cold- and warm-end biases.

The cold-end biases reported here are used in the XCAL "CC" version 1.1 [13], but currently, CC v1.1 does not use the reported CFRSL warm-end values. In future, we expect that the CFRSL warm-end biases will be included, and subsequently, the CC v1.1 will be updated.

ACKNOWLEDGMENT

The authors would like to acknowledge the useful comments offered by three anonymous reviewers.

REFERENCES

[1] J. Hollinger, Ed., *DMSP Special Sensor Microwave Imager Calibration/Validation—Final Report*. Washington, DC: Naval Res. Lab., Jul. 1989.
[2] J. Hollinger, J. Peirce, and G. Poe, "SSM/I instrument evaluation," *IEEE Trans. Geosci. Remote Sens.*, vol. 28, no. 5, pp. 781–790, Sep. 1990.
[3] J. Hollinger, Ed., *DMSP Special Sensor Microwave Imager Calibration/Validation—Final Report*. Washington, DC: Naval Res. Lab., May 1991.
[4] M. Colton and G. Poe, "Intersensor calibration of DMSP SSM/I's: F-8 to F-14, 1987–1997," *IEEE Trans. Geosci. Remote Sens.*, vol. 37, no. 1, pp. 418–439, Jan. 1999.
[5] Remote Sensing Systems. [Online]. Available: http://www.remss.com/
[6] F. Wentz, P. Ashcroft, and C. Gentemann, "Post-launch calibration of the TRMM microwave imager," *IEEE Trans. Geosci. Remote Sens.*, vol. 39, no. 2, pp. 415–422, Feb. 2001.
[7] T. Meissner and F. Wentz, "Intercalibration of AMSR-E and Windsat brightness temperature measurements over land scenes," in *Proc. IEEE IGARSS*, Jul. 2010, pp. 3218–3219.
[8] F. Wentz, "Inter-calibration of SSM/I F13, SSM/IS F16, and WindSat: A holistic approach (Invited)," *EOS Trans. AGU*, vol. 19, no. 26, 2010>, Ocean Sci. Meet. Suppl., Abstract IT24A-01.
[9] P. Gaiser, K. St Germain, E. Twarog, G. Poe, W. Purdy, D. Richardson, W. Grossman, W. Jones, D. Spencer, G. Golba, J. Cleveland, L. Choy, R. Bevilacqua, and P. Chang, "The Windsat spaceborne polarimetric microwave radiometer: Sensor description and early orbit performance," *IEEE Trans. Geosci. Remote Sens.*, vol. 42, no. 11, pp. 2347–2361, Nov. 2004.
[10] L. Hong, "Inter-satellite microwave radiometer calibration," Ph.D. dissertation, Sch. Elect. Eng. Comput. Sci., Univ. Central Florida, Orlando, FL, 2008.
[11] L. Hong, W. L. Jones, T. T. Wilheit, and T. Kasparis, "Two approaches for inter-satellite radiometer calibrations between TMI and WindSat," *J. Meteorol. Soc. Jpn.*, vol. 87A, pp. 223–235, 2009.
[12] T. T. Wilheit, private communication, 2007.

[13] T. Wilheit, W. Berg, L. Jones, R. Kroodsma, D. McKague, C. Ruf, and M. Sapiano, "A consensus calibration based on TMI and WindSat," in *Proc. IEEE IGARSS*, Jul. 2011, pp. 2641–2644.
[14] S. T. Brown and C. S. Ruf, "Determination of an Amazon hot reference target for the on-orbit calibration of microwave radiometers," *J. Atmos. Ocean. Technol.*, vol. 22, no. 9, pp. 1340–1352, Sep. 2005.
[15] C. Kummerow, W. Barnes, T. Kozu, J. Shiue, and J. Simpson, "The Tropical Rainfall Measuring Mission (TRMM) sensor package," *J. Atmos. Ocean. Technol.*, vol. 15, no. 3, pp. 809–817, Jun. 1998.
[16] GES DISC Webpage for TMI 1B11 Data. [Online]. Available: http://mirador.gsfc.nasa.gov/collections/TRMM_1B11__007.shtml
[17] K. Gopalan, L. Jones, S. Biswas, S. Bilanow, T. Wilheit, and T. Kasparis, "A time-varying radiometric bias correction for the TRMM microwave imager," *IEEE Trans. Geosci. Remote Sens.*, vol. 47, no. 11, pp. 3722–3730, Nov. 2009.
[18] S. Biswas, K. Gopalan, W. Jones, and S. Bilanow, "Correction of time-varying radiometric errors in TRMM microwave imager calibrated brightness temperature products," *IEEE Geosci. Remote Sens. Lett.*, vol. 7, no. 4, pp. 851–855, Oct. 2010.
[19] GES DISC Mirador Earth Science Data Search Tool. [Online]. Available: http://mirador.gsfc.nasa.gov/
[20] T. Lungu, Ed., "Sensor Data Record Files (SDR)," in *WindSat Data Products Users' Manual: Sensor and Environmental Data Records*. Pasadena, CA: Jet Propulsion Lab., Jan. 2006, Version 3.0, D-29825.
[21] NCEP (National Centers for Environmental Prediction) FNL (Final) Operational Global Analyses. [Online]. Available: http://rda.ucar.edu/datasets/ds083.2/
[22] D. P. Dee, S. M. Uppala, A. J. Simmons1, P. Berrisford, P. Poli, S. Kobayashi, U. Andrae, M. A. Balmaseda, G. Balsamo, P. Bauer, P. Bechtold, A. C. M. Beljaars, L. van de Berg, J. Bidlot, N. Bormann, C. Delsol, R. Dragani, M. Fuentes, A. J. Geer, L. Haimberger, S. B. Healy, H. Hersbach, E. V. Hólm, L. Isaksen, P. Kållberg, M. Köhler, M. Matricardi, A. P. McNally, B. M. Monge-Sanz, J.-J. Morcrette, B.-K. Park, C. Peubey, P. de Rosnay, C. Tavolato, J.-N. Thépaut, and F. Vitart, "The ERA-Interim reanalysis: Configuration and performance of the data assimilation system," *Q. J. R. Meteorol. Soc.*, vol. 137, no. 656, pp. 553–597, Apr. 2011.
[23] T. Meissner and F. Wentz, "The complex dielectric constant of pure and sea water from microwave satellite observations," *IEEE Trans. Geosci. Remote Sens.*, vol. 42, no. 9, pp. 1836–1849, Sep. 2004.
[24] G. Elsaesser, "A parametric optimal estimation retrieval of the nonprecipitating parameters over the global oceans," M.S. thesis, Colorado State Univ., Fort Collins, CO, 2006.
[25] T. Wilheit, "A model for the microwave emissivity of the ocean's surface as a function of wind speed," *IEEE Trans. Geosci. Electron.*, vol. GE-17, no. 4, pp. 244–249, Oct. 1979.
[26] J. Hollinger, "Passive microwave measurements of sea surface roughness," *IEEE Trans. Geosci. Electron.*, vol. GE-9, no. 3, pp. 165–169, Jul. 1971.
[27] A. Stogryn, "The emissivity of sea foam at microwave frequencies," in *Proc. Antennas Propag. Soc. Int. Symp.*, Sep. 1971, vol. 9, pp. 169–171.
[28] F. Wentz, "Measurement of oceanic wind vector using satellite microwave radiometers," *IEEE Trans. Geosci. Remote Sens.*, vol. 30, no. 5, pp. 960–972, Sep. 1992.
[29] P. W. Rosenkranz, "Water vapor microwave continuum absorption: A comparison of measurements and models," *Radio Sci.*, vol. 33, no. 4, pp. 919–928, 1998.
[30] H. J. Liebe, G. A. Hufford, and T. Manabe, "A model for the complex permittivity of water at frequencies below 1 THz," *Int. J. Infrared Millim. Waves*, vol. 12, no. 7, pp. 659–675, Jul. 1991.
[31] H. Liebe, P. Rosenkranz, and G. Hufford, "Atmospheric 60-GHz oxygen spectrum: New laboratory measurements and line parameters," *J. Quantitative Spectrosc. Radiat. Transf.*, vol. 48, no. 5/6, pp. 629–643, 1992, Special Issue Conference on Molecular Spectroscopic Databases.
[32] P. W. Rosenkranz, "Absorption of microwaves by atmospheric gases," in *Atmos. Remote Sensing By Microwave Radiometry*, M. A. Janssen, Ed. Hoboken, NJ: Wiley, 1993, p. 37.
[33] T. Wilheit, XCAL Models Used. [Online]. Available: http://gpm-x-cal.info/orig_models.pdf
[34] B. Geerts and E. Linacre, The Height of the Tropopause, 1997. [Online]. Available: http://www-das.uwyo.edu/~geerts/cwx/notes/chap01/tropo.html
[35] M. Wisler and J. Hollinger, "Estimation of Marine Environmental Parameters Using Microwave Radiometric Remote Sensing Systems," Naval Res. Lab., Washington, DC, NRL Memorandum Rep. 3661, 1977, Defense Tech. Inf. Center.
[36] F. Karbou and C. Prigent, "Calculation of microwave land surface emissivity from satellite observations: Validity of the specular approximation over snow-free surfaces?" *IEEE Geosci. Remote Sens. Lett.*, vol. 2, no. 3, pp. 311–314, Jul. 2005.
[37] T. Ingold, R. Peter, and N. Kampfer, "Weighted mean tropospheric temperature and transmittance determination at millimeter-wave frequencies for ground-based applications," *Radio Sci.*, vol. 33, no. 4, pp. 905–918, 1998.
[38] C. Matzler, "Applications of the interaction of microwaves with the natural snow cover," *Remote Sens. Rev.*, vol. 2, no. 12, pp. 259–387, 1987.
[39] F. T. Ulaby, R. K. Moore, and A. K. Fung, *Microwave Remote Sensing: Active and Passive*. Norwood, MA: Artech House, 1981.
[40] R. Isaacs, Y.-Q. Jin, R. Worsham, G. Deblonde, and V. J. Falcone, "The RADTRAN microwave surface emission models," *IEEE Trans. Geosci. Remote Sens.*, vol. 27, no. 4, pp. 433–440, Jul. 1989.
[41] P. Ferrazzoli and L. Guerriero, "Passive microwave remote sensing of forests: A model investigation," *IEEE Trans. Geosci. Remote Sens.*, vol. 34, no. 2, pp. 433–443, Mar. 1996.
[42] D. McKague, C. Ruf, and J. Puckett, "Beam spoiling correction for spaceborne microwave radiometers using the two-point vicarious calibration method," *IEEE Trans. Geosci. Remote Sens.*, vol. 49, no. 1, pp. 21–27, Jan. 2011.
[43] C. Ruf, "Detection of calibration drifts in spaceborne microwave radiometers using a vicarious cold reference," *IEEE Trans. Geosci. Remote Sens.*, vol. 38, no. 1, pp. 44–52, Jan. 2000.

Sayak K. Biswas (S'08–M'12) received the B.Tech. degree in electronics and communication engineering from the National Institute of Technology, Calicut, India, in 2005 and the M.S. and Ph.D. degrees in electrical engineering from the University of Central Florida (UCF), Orlando, in 2009 and 2012, respectively.

He is currently a National Aeronautics and Space Administration (NASA) Postdoctoral Fellow with the Earth Science Office at the Marshall Space Flight Center in Huntsville, AL. From 2008 to early 2012, he was with the Central Florida Remote Sensing Laboratory (CFRSL) at UCF, where he contributed in various research projects related to the calibration of microwave radiometers and geophysical retrieval algorithm development from microwave radiometer data. His major contributions include the following: the implementation and validation of a time-varying radiometric bias correction algorithm in the version 7 of the Tropical Rainfall Measurement Mission Microwave Imager 1B11 data product, the computation of intersensor bias between various satellite radiometers for Global Precipitation Measurement consensus calibration standard development, the Argentine Space Agency Comision Nacional De Actividades Espaciales (CONAE)'s microwave radiometer calibration and prelaunch geophysical retrieval algorithm development, wind speed and rain rate retrieval algorithm development for the Hurricane Imaging Radiometer during the NASA Genesis and Rapid Intensification Processes (GRIP) field campaign, and also postflight data analysis, geolocation, and validation. Prior to CFRSL, he was a Tutor employed by the Electrical Engineering Department at UCF to help undergraduate students in basic electrical engineering courses. From 2005 to 2007, he worked as an Associate Systems Engineer at IBM India Private Ltd., Pune, India.

Dr. Biswas is a recipient of the NASA Postdoctoral Research Fellowship Award for the proposal titled "Calibration and Image Reconstruction Algorithm Development for Hurricane Imaging Radiometer."

Spencer Farrar (S'07) received the B.S. and M.S. degrees in electrical engineering from the University of Central Florida, Orlando, in 2008 and 2009, respectively. He is currently working toward the Ph.D. degree in electrical engineering at the University of Central Florida.

Since 2008, he has been a Graduate Research Assistant with the Central Florida Remote Sensing Laboratory, University of Central Florida. His past research within the satellite remote sensing field has been intersatellite calibration, radiometer cold sky analysis, and signal processing.

Kaushik Gopalan received the B.E. degree in electronics and communication from the Rashtreeya Vidyalaya College of Engineering, Bangalore, India, in 2003 and the M.S. and Ph.D. degrees in electrical engineering from the University of Central Florida, Orlando, in 2005 and 2008, respectively.

From 2008 to 2011, he was a Researcher with the Earth System Science Interdisciplinary Center, University of Maryland, College Park. He is currently with the Space Applications Center, Ahmedabad, India.

Andrea Santos-Garcia (S'12) received the B.S. degree in electronic engineering from the Universidad Industrial de Santander, Bucaramanga, Colombia, in 2005 and the M.S. degree in electrical engineering from the University of Puerto Rico, Mayaguez, in 2010. She is currently working toward the Ph.D. degree in electrical engineering from the University of Central Florida, Orlando.

Since summer 2011, she has been a Graduate Research Assistant at Central Florida Remote Sensing Laboratory at the University of Central Florida in Orlando. Prior to that, she was working in the oil industry from 2006 to 2007. Then, she was a Graduate Research Assistant at the Laboratory for Applied Remote Sensing and Image Processing at the University of Puerto Rico from 2008 to 2010. Her research includes satellite remote sensing, signal processing, image processing, and biomedical applications. Her current focus is on intersatellite radiometric calibration/validation, microwave radiative transfer modeling, and digital signal processing.

Mrs. Santos-Garcia has served as a reviewer for the IEEE Workshop on Hyperspectral Image and Signal Processing: Evolution in Remote Sensing, and she is a student member of SPIE.

W. Linwood Jones (SM'75–F'99–LF'09) received the B.S. degree in electrical engineering from the Virginia Polytechnic Institute, Blacksburg, in 1962, the M.S. degree in electrical engineering from the University of Virginia, Charlottesville, in 1965, and the Ph.D. degree in electrical engineering from the Virginia Polytechnic Institute and State University, Blacksburg, in 1971.

He is currently a Professor with the Department of Electrical and Computer Engineering, University of Central Florida (UCF), Orlando. At UCF, he teaches undergraduate and graduate courses in radio frequency (RF)/microwave (MW) communications, satellite remote sensing, and radar systems. Also, he is the Director of the Central Florida Remote Sensing Laboratory, where he performs research in satellite microwave remote sensing technology development. Prior to becoming a College Professor in 1994, he had 27 years of federal government employment with National Aeronautics and Space Administration (NASA) at the Langley Research Center in Hampton, VA; at NASA Headquarters in Washington DC; and at the Kennedy Space Center, FL. Furthermore, he spent eight years in the private aerospace industry with employment at General Electric's Space Division in King of Prussia, PA, and Harris Corporation's Government Aerospace Systems Division in Melbourne, FL.

Dr. Jones is a Life Fellow of the IEEE Geoscience and Remote Sensing Society, Antennas and Propagation Society, and Oceanic Engineering Society and a member of the American Geophysical Union and Commission F of the Union Radio Scientifique Internationale. For excellence in education, he received the IEEE Orlando Section: Outstanding Engineering Educator Award 2003, the College of Engineering: Excellence in Undergraduate Teaching Award 2004, the IEEE Florida Council: Outstanding Engineering Educator Award 2004, and the University of Central Fl Outstanding Graduate Student Mentor Award 2011. For his research, he received four NASA Special Achievement Awards, eight NASA Group Achievement Awards, the Centre National d'Etudes Spatiales (CNES) Space Medal, the Aviation Week and Space Technology Space Program Award 1993, and the Naval Research Laboratory 2004 Alan Berman Research Publications Award.

Stephen Bilanow received the B.S. degree in physics from the University of Massachusetts, Amherst, in 1979.

He has worked for companies in support of the NASA Goddard Space Flight Center for over 30 years, being involved with spacecraft flight dynamics support, attitude sensor calibration error analysis, geolocation analysis, and science instrument calibration. He supported the Tropical Rainfall Measuring Mission since before the launch and is currently supporting the Global Precipitation Measurement Precipitation Processing System. He is currently with Wyle Information Systems, McLean, VA.